JOURNAL OF COMPUTATIONAL PHYSICS 60, 489–516 (1985)

Wave-Induced Bed Flows by a Lagrangian Vortex Scheme

P. A. SMITH AND P. K. STANSBY

Simon Engineering Laboratories, University of Manchester, Manchester, England

Received June 7, 1984; revised December 11, 1984

Nominally 2-dimensional viscous flow induced by gravity waves over a spatially periodic bed is simulated by a Lagrangian vortex scheme. A vortex sheet is introduced on the surface at each time step to satisfy the zero velocity conditions. The sheet is discretised; the vortex-in-cell method is used to convect vorticity and random walks are added to effect viscous diffusion. Good agreement with analytical theory is obtained for velocity profiles in uniform sinusoidal flow and for mass transport due to linear waves. Mass transport for finite amplitude waves is also obtained. For separated flow over rippled beds, which is still liminar, a vortex decay factor is required to produce agreement with experiment and is thought to compensate for large scale 3-dimensional effects. © 1985 Academic Press, Inc.

INTRODUCTION

The solution of the vorticity equation by the Lagrangian discrete-vortex method presented by Chorin [1, 2] represents an attractive alternative to Eulerian finite-difference schemes [3]. In particular, a solid surface is not required to follow a mesh contour. The vorticity is represented as points of concentrated circulation, vortices, which are convected in an inviscid calculation, and viscous diffusion is superimposed by adding random walks. This representation improves as the number of vortices increases, and to obtain efficient velocity calculations for very large numbers of vortices (up to 10^4) Stansby and Dixon [4] incorporated the use of the vortex-in-cell method [5, 6, 7]. They tested the method with steady and oscillatory onset flow on a circular cylinder and showed good qualitative agreement with experiment. In this paper, this approach is applied to laminar, wave-induced flows on a plane and slightly undulating bed, where flow is attached, and on a rippled bed, where flow is separated. For the former, there is an analytical solution for mass transport due to linear waves and for the latter, there are accurate measurements of periodic velocity fluctuation. The only previous comparison with an analytical solution was for steady flow over a flat plate (without using the vortex-in-cell method). These flows are thus rather different with a strong oscillation and a zero or weak mean component; vertical convective motion is of vital importance. Mass transport is also obtained for waves of finite amplitude [2] (defined by an accurate numerical method [8]) which is of some practical value in the field of coastal engineering. The

0021-9991/85 $3.00

method is first tested with a uniform sinusoidal onset flow over a plane bed, so that velocity profiles may be compared with Stokes theory [9]. This is also the onset flow used in the rippled bed measurements. In principle an arbitrary wave flow may be used to drive mass transport with flow separation, but this has not been attempted here.

Theoretical Formulation

Discrete Vortex Method

A Lagrangian vortex scheme may be used to solve the vorticity equation for 2-dimensional flows:

$$\frac{D\omega}{Dt} = \nu\nabla^2\omega. \tag{1}$$

At the onset of any flow, a surface may be represented by a vortex sheet, with a variation of intensity chosen so that the velocity everywhere inside the surface is zero. After a time step Δt, the action of viscosity diffuses vorticity from the surface into the fluid. This may be modelled by applying random disturbances to the sheet, represented as a layer of discrete vortices, the orthogonal co-ordinates of the ith vortex in the sheet changing according to the equations:

$$x_i(t+\Delta t) = x_i(t) + \eta_{1i}(t) \tag{2a}$$

$$y_i(t+\Delta t) = y_i(t) + \eta_{2i}(t). \tag{2b}$$

A set of random numbers is sampled at each time step from a Gaussian distribution with zero mean and variance $2\nu\Delta t$, where ν is the kinematic viscosity. The values of $\eta_{1i}(t)$ and $\eta_{2i}(t)$ are read consecutively from this set. Any vortex passing below the the surface is reflected back onto its mirror-image position in the fluid [2, 4].

To determine the convective component of motion, the velocity for each vortex may be calculated by summing the contributions of every other vortex in the flow. The time taken to perform this calculation becomes prohibitively high when large numbers of vortices have been introduced (>200 say). An efficient alternative is provided by the vortex-in-cell method, described below. At each new time step the surface boundary condition is maintained by creating a new vortex sheet along the surface.

Vortex-in-Cell Method

The velocity (u, v) at any point can be obtained from the vorticity distribution using Poisson's equation, which relates vorticity ω to stream function ψ

$$\nabla^2\psi = -\omega, \tag{3}$$

together with the equation

$$u = \frac{\partial \psi}{\partial y} \tag{4a}$$

$$v = -\frac{\partial \psi}{\partial x}. \tag{4b}$$

These equations are solved on a rectangular mesh, defined over the region of rotational flow. Each discrete vortex contributes to the vorticity at the four mesh points of the cell in which it is situated. An area weighting scheme was used, which conserves total circulation.

Poisson's equation (3) can be solved efficiently by the use of fast Fourier transforms, yielding the stream function distribution. A routine for this purpose was available at the University of Manchester Regional Computer Center (UMRCC). Equation (4), expressed in finite difference form, may then be used to calculate the velocity at any mesh point where it is required:

$$u_{i,j} = (\psi_{i,j+1} - \psi_{i,j-1})/2\Delta y \tag{5a}$$

$$v_{i,j} = -(\psi_{i+1,j} - \psi_{i-1,j})/2\Delta x \tag{5b}$$

Δx and Δy are the dimensions of the mesh in x and y, respectively. The local velocity of each discrete vortex can be found, by bilinear interpolation, from the velocities of the four mesh points of the cell which contains it.

The vortices are moved according to a second-order scheme:

$$x(t+\Delta t) = x(t) + (u(t) + u'(t))\,\Delta t/2 \tag{6a}$$

$$y(t+\Delta t) = y(t) + (v(t) + v'(t))\,\Delta t/2 \tag{6b}$$

where $u'(t)$ and $v'(t)$ are the velocities at position (x', y'):

$$x'(t) = x(t) + u(t)\,\Delta t \tag{7a}$$

$$y'(t) = y(t) + v(t)\,\Delta t. \tag{7b}$$

Boundary Conditions for the Mesh

The orthogonal coordinates x and y are defined to be, respectively, tangential and normal to the bed. A rectangular region R, with boundaries B_1, B_2, B_3, and B_4 is set up so that the surface lies parallel to B_1 and B_3 (Fig. 1). The region contains the mesh on which Poisson's equation (3) is solved, the following set of boundary conditions having been specified:

(i) Periodic boundary conditions are imposed on B_4 and B_2; their separation L_x is equal to the wavelength, if any, of the flow.

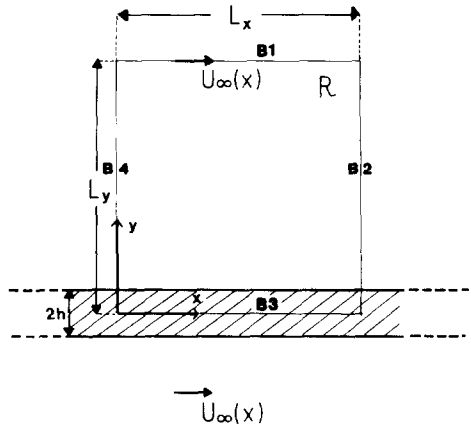

FIG. 1. Flow region for the solution of Poisson's equation.

(ii) $\partial\psi/\partial y$ is specified along B_1. If L_y-h is sufficiently large, this can be equated to the free-stream velocity $u_\infty(x)$:

$$\frac{\partial\psi}{\partial y} = u_\infty(x). \tag{8}$$

(iii) If the plane bed is considered to be the upper face of a body of infinite extent in the x direction, with thickness $2h$ and with a line of symmetry along $y = 0$, the normal component of velocity will, by symmetry, be zero along $y = 0$ (Fig. 1). ψ can thus be set equal to an arbitrary constant at all points along B_3.

It is a feature of the vortex-in-cell method that the influence of vortices within one cell size of a surface is not accurately represented at the surface [4, 7]. Tangential surface velocities, required in the calculation of the strengths of new vortex sheets, are thus calculated at a distance of one cell size (Δy) inside the surface. From Eq. (5b), this sets a lower limit of $4\Delta y$ on the value of $2h$.

The Expanding Mesh

In order to model the boundary layer in detail, while maintaining B_1 above the region of rotational flow, a mesh may be used which expands exponentially in the y direction. A change of variable is introduced, i.e.,

$$y' = A \ln(y + 1) \tag{9}$$

where A determines the rate of expansion of the mesh. This is equivalent to mapping the mesh points of the expanding mesh onto a uniform rectangular mesh. The routine used to solve Eq. (3) was modified to solve equations of the form:

$$\frac{d^2\psi}{dx^2} + a(y')\frac{d^2\psi}{dy'^2} + b(y')\frac{d\psi}{dy'} = -\omega. \tag{10}$$

Applying the change of variable (9) to Poisson's equation (3),

$$a(y') = A^2 \exp(-2y'/A) \tag{11a}$$

$$b(y') = -A \exp(-2y'/A). \tag{11b}$$

The boundary condition specified along B_1 (Eq. (9)) must also be modified:

$$\left(\frac{d\psi}{dy'}\right)_1 = \frac{\exp(y'/A)\, u_1(x)}{A} \tag{12}$$

where suffix 1 corresponds to values taken along B_1, the top of the mesh.

The Influence Matrix

In the case of a infinite plane, the velocity beneath the surface becomes zero if the new vortex sheet strength is simply made equal to twice the local tangential component of the surface velocity; vortex sheet elements are collinear and have no influence on each other. For an infinite rectangular body (Fig. 1), however the influence of the vortex sheet representing the lower surface of the body must be taken into account.

Vortex sheet strength may be determined from the distribution of tangential velocities which would exist along the surface in the absence of the sheet. The strength of any finite segment may be obtained numerically by solving the matrix equation

$$\mathbf{K}\boldsymbol{\gamma} = \mathbf{b} \tag{13}$$

where

$$K(I, J) = \frac{1}{2\pi}\left[\int_{s_A}^{s_B} (\nabla_p \wedge \ln(r_s)\,\mathbf{k}) \cdot \mathbf{t}_p \, ds\right] \qquad (I \neq J)$$

$$K(I, J) = 0.5 \qquad (I = J)$$

$$b(I) = -\mathbf{u}_p^t.$$

The surface of the body, which lies in the (x, y) plane, is parameterised by a variable s. s_A and s_B are the end points of the Jth segment. r_s is the distance between an arbitrary origin and a point on the Jth segment. $\mathbf{k}$ is the unit vector in the z direction and $\mathbf{t}_p$ is the tangential unit vector at P, a collocation point at the midpoint of the Ith segment. $\mathbf{u}_p^t$ is the tangential velocity at P in the absence of surface vorticity. $\gamma(I)$ is the strength of the Ith segment (assumed to be uniform). If $\mathbf{K}$ is non-singular, a solution for γ is given by

$$\boldsymbol{\gamma} = (\mathbf{K}^{-1})\,\mathbf{b}. \tag{14}$$

The element $K(I, J)$ $(I \neq J)$ is equivalent to the tangential velocity which would be

induced at the collocation point of segment I by the Jth segment, if the Jth segment were to have unit strength. This quantity is dependent only upon the geometry of the body; $\mathbf{K}^{-1}$, the influence matrix, need only be calculated once and then stored. At each time step, the surface vorticity distribution can be found by postmultiplication with $\mathbf{b}$.

Two approaches have been adopted in calculating $K(I, J)$ for an infinite plane modelled as a rectangular body of infinite length and finite thickness:

(i) approximating each segment by a point vortex and using the exact expession for the velocity due to an infinite row of vortices [10].

(ii) applying the exact expression for the velocity field of a single vortex sheet, but truncating the series at some distance on either side of I.

The errors in approach (i) will tend to decrease as the separation between the upper and lower surfaces increases. The converse is true of approach (ii), as is illustrated in Fig. 2. The separation is determined by the mesh size in the y direction and therefore by the normal extent of rotational flow, the boundary layer thickness. The selection of either (i) or (ii) thus depends upon the ratio of the boundary layer thickness to the wavelength of the flow.

To model infinite surfaces of general periodic form, terms representing the influence of the upper surface are of course significant.

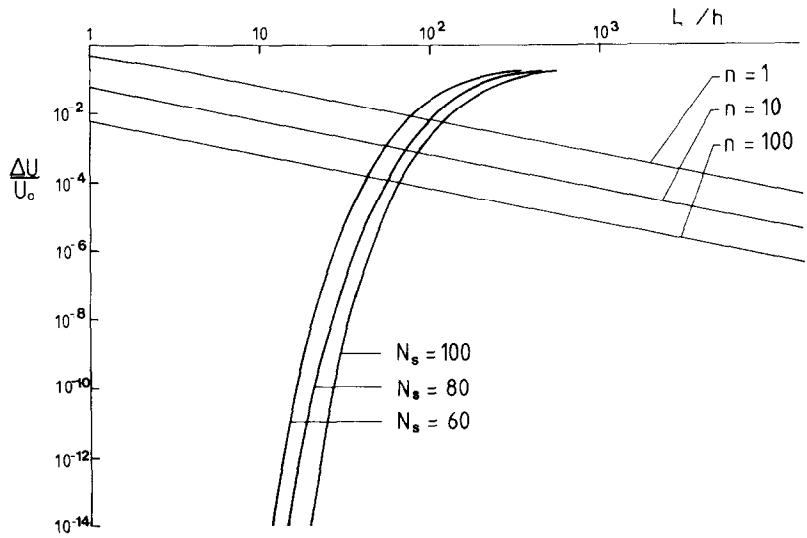

FIG. 2. The calculation of steady, irrotational flow, velocity U_0, over a plane, represented by: (i) an infinite row of point vortices, each separated by a distance L_x/N_s; (ii) a finite row of linear vortex sheets, of total length nL_x. The error in horizontal velocity Δu at a height h above the plane, for methods (i) and (ii), respectively, is given by: $\Delta U/U_0 = (2\exp(-\lambda) - 1)/(\exp(\lambda) + \exp(-\lambda) - 1)$, $\lambda = 2\pi h N_s/L_x$ (heavy line); and $\Delta U/U_0 = 1 - (2/\pi)\arctan(nL_x/h)$(light line).

Sinusoidal Flow over a Plane Bed

In order to assess certain numerical parameters and to test the accuracy of the method, results were compared with the analytical solution for a fluid executing linear sinusoidal oscillations parallel to an infinite plane. If the free stream velocity u of the fluid varies sinusoidally as a function of time ($U_0 \sin(\sigma t)$), the flow will reach a steady state in which vorticity is confined to a boundary layer of thickness $O(\delta)$, where $\delta = (2\nu/\sigma)^{1/2}$. The velocity profile is given by

$$u/U_0 = \sin(\sigma t) - \exp(-y/\delta)\sin(\sigma t - y/\delta). \tag{15}$$

For a particular value of y/δ, the quantity u/U_0 is independent of the amplitude of oscillation, expressed in the form of a Reynolds number

$$\mathrm{Re} = U_0^2/(\nu\sigma).$$

A uniform rectangular mesh was used for the velocity calculation. B_1, the upper boundary of the mesh, was set at a distance of 5.1δ above the surface. In the analytical solution for the steady-state flow, a maximum of 0.59% of the total vorticity should lie outside the domain of the calculation. The boundary condition (Eq. (8)), imposed along $B1$ in the solution of Poisson's equation (Eq. (3)), was

$$\frac{\partial \psi}{\partial y} = U_0 \sin(\sigma t) + \sum_{y_i > y} \frac{\Gamma_i}{L_x} \tag{16}$$

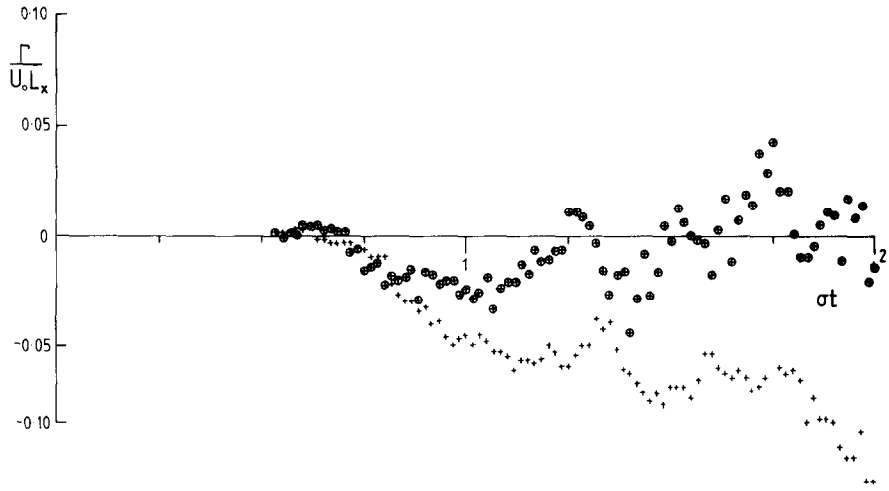

FIG. 3. Time variation of $\Gamma/U_0 L$ following the onset of flow. Γ is the total circulation within the fluid above the mesh. Discrete vortices, having passed through the upper boundary of the mesh, may either (i) be held stationary (+) or (ii) be allowed to continue their random walk (⊕), thereby having a finite probability of reentering the mesh.

in which the final term incorporates into the calculation the influence of discrete vortices which have diffused above B_1. Viscous diffusion, modelled by Eq. (2), is applied to all of the discrete vortices. Fig. 3 illustrates that it is necessary to include those vortices lying outside the mesh in order to prevent the occurrence of a systematic error, leading to a steady accumulation of circulation above B_1.

The time development of velocity profiles during the first two cycles following the onset of the flow is shown in Fig. 4 for $\mathrm{Re} = 100$ and $\mathrm{Re} = 0$. At $\mathrm{Re} = 100$, the amplitude of the convective motion of the vortices exceeds that due to viscous diffusion. At $\mathrm{Re} = 0$, $\nu \to \infty$ and $\sigma \to \infty$ while the ratio ν/σ, and therefore the viscous diffusion of the vortices, remains finite. The amplitude of convective motion U_0/σ, however, tends to zero.

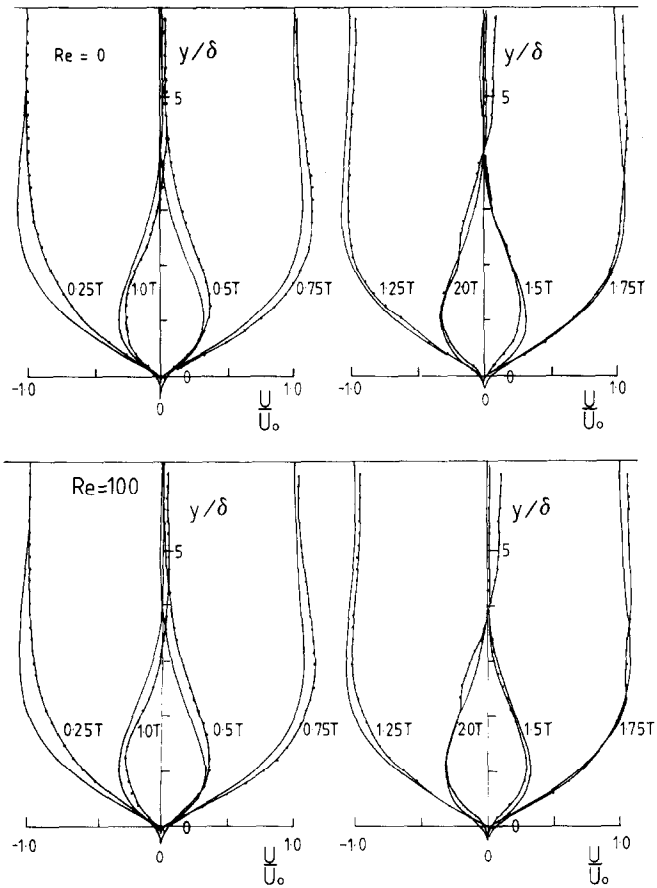

FIG. 4. Time development of velocity profiles above a plane surface following the onset of sinusoidal wave motion, for which $\mathrm{Re} = 0$ and $\mathrm{Re} = 100$: (—) = steady-state solution (Stokes); (···) = computational results.

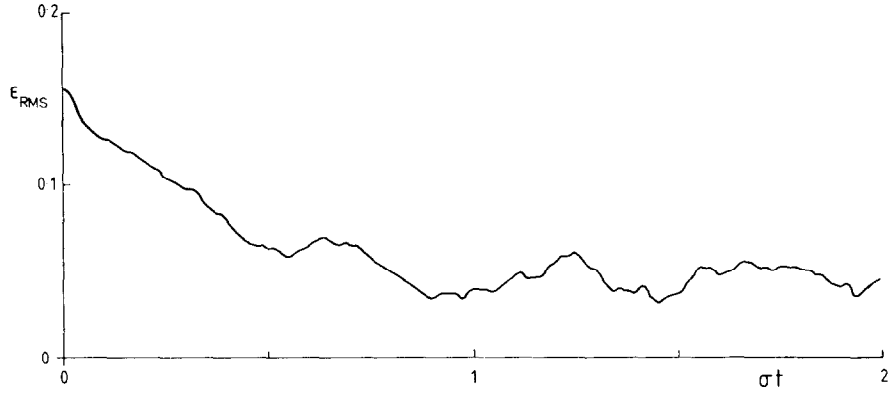

FIG. 5. Time variation of the r.m.s. error in the velocity profile of sinusoidal flow over a plane, for the case of $\mathrm{Re} = 0$.

An rms error in the computed velocity profile is defined as

$$\varepsilon_{\mathrm{rms}}(t) = \frac{1}{U_0 y_1}\left[\int_0^{y_1} (u_c(y, t) - u_T(y, t))^2 \, dy\right]^{1/2} \tag{17}$$

where u_c and u_T are respectively the computed and theoretical velocities at time t. $\varepsilon_{\mathrm{rms}}$ reaches an approximately constant value after the first cycle (Fig. 5). It can be used to make a quantitative comparison of computed and theoretical velocity profiles as the parameters of the mesh and the flow are varied.

Figure 6 show $\varepsilon_{\mathrm{rms}}$ evaluated at the end of the first cycle, plotted against Reynolds number. Its value varies by less than 5% over the range of Reynolds number $0 < \mathrm{Re} < 10^4$. Above this range, however, it increases continuously. The increase in $\varepsilon_{\mathrm{rms}}$ at high Reynolds numbers is the result of errors in the calculation of v, the velocity component normal to the plane. This produces normal displacements of the discrete vortices, the magnitude of which becomes comparable to δ as the relative thickness of the boundary layer decreases.

In Fig. 7, the effect is shown of varying the cell size parallel to the plane (Δx) at three different Reynolds numbers. The results are consistent with Fig. 6: greater errors are found for flows in which amplitude is large with respect to boundary layer thickness. This is only true, however, when the tangential displacement of the

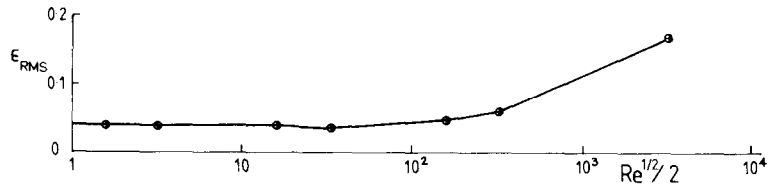

FIG. 6. The variation in r.m.s. error, evaluated at the end of the first cycle, with $\mathrm{Re}^{1/2}/2$.

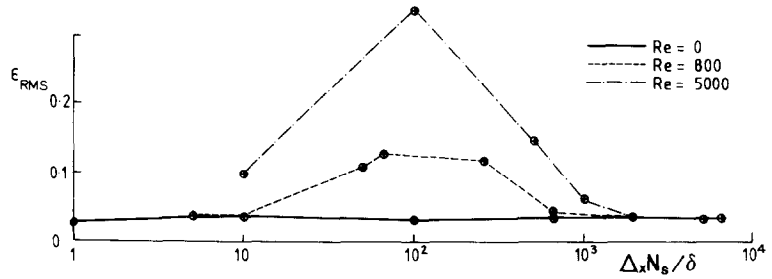

FIG. 7. The variation in r.m.s. error, evaluated at the end of the first cycle with $\Delta x N_s/\delta$.

discrete vortices in one time step is greater than the cell size Δx. At higher values of Δx, errors are independent of the Reynolds number.

Appropriate values for the parameters $T/\Delta t$, y_1/δ, $L_x/\Delta x$, and N_S, where N_S is the number of vortex sheets representing the section of the plane covered by the mesh, are given below:

$$\frac{T}{\Delta t} \gtrsim 40 \tag{18a}$$

$$\frac{y_1}{\delta} \gtrsim 5 \tag{18b}$$

$$\frac{L_x}{\Delta x} \gtrsim 33 \tag{18c}$$

$$N_s \gtrsim 60 \tag{18d}$$

The results on which (18d) is based are plotted in Fig. 8.

MASS TRANSPORT

Physical Background

Mass transport under gravity waves is the long-term drift of fluid elements. Stokes [11] made the first theoretical study of mass-transport velocity, in which he

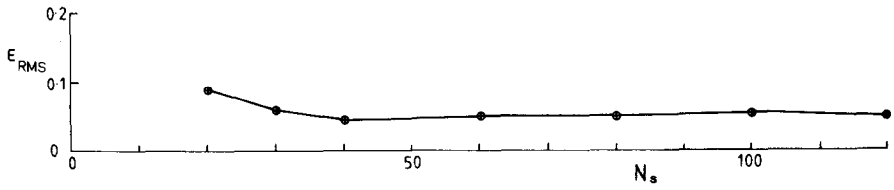

FIG. 8. The variation in r.m.s. error, evaluated at the end of the first cycle, with N_s.

considered small amplitude progressive waves, assuming irrotational flow throughout the fluid. In contrast to observation, Stokes theory predicts a mass-transport velocity at the bed in the opposite direction to that of propagation of the wave.

A forward mass transport in the lower part of the flow was obtained, to a first approximation, by Longuet-Higgins [12], whose theory included the effects of viscous boundary layers at the free surface and at the bottom. Longuet-Higgins considered both standing waves and progressive waves of infinite lateral extent. Motions in the interior and in the boundary layers were dealt with separately. At the bottom, the mass transport velocity tends towards a limiting value just beyond the boundary layer, whereas at the free surface the same is true of its gradient. These results are independent of the ratio of amplitude of particle motion (wave amplitude) a to boundary-layer thickness δ. In the interior, however, the nature of the motion is determined by this ratio. When $a \ll \delta$, viscous diffusion governs the distribution of vorticity, whereas when $a \gg \delta$, vorticity is diffused with the mass-transport velocity. The corresponding solutions to the field equations were called the conduction and convection solutions. The conduction solution is unique when the net mass flow acoss any vertical section is specified. The convection solution, however, requires the specification of additional boundary conditions at the upstream and downstream ends of the flow.

Dore [13] derived the mass-transport velocity for linear waves in which $a \gg \delta$ by the use of a double boundary-layer model. The double boundary layers consist of oscillatory boundary layers, of thickness δ, at the bottom and at the free surface, inside which first-order vorticity is confined. Adjacent to these are the outer boundary layers, of greater thickness, which contain the second-order vorticity. The assumption of infinite lateral extent is no longer made; the waves are assumed to be generated at a point $x = 0$, and to commence at a time $t = 0$. After a sufficient time has elapsed, and at a sufficient distance from $x = 0$, a steady-state vorticity field becomes established within the boundary layers and the corresponding mass-transport velocity can be derived.

Several theoretical investigations have concentrated on the bottom boundary layer; the mass-transport velocity in this region is of particular interest because of its role in the motion of sediment near the sea bed. Dore [14] obtained a second-order approximation to the mass-transport velocity, taking into account the development of an outer boundary layer and the point of generation of the waves. The effect is to impose a uniform shear velcoity, which decays as $(1/x)^{1/2}$, on the solution of Longuet-Higgins. In the case of progressive waves, this gives a reduction in the mass-transport velocity compared to the predictions of first-order theory; this reduction tends to zero as x tends to infinity.

Isaacson [15] had earlier obtained a first approximation to mass-transport velocity for shallow water waves at the edge of the bottom boundary layer, based on cnoidal wave theory. In 1978 [16], he produced a series of curves based on cnoidal theory and Stokes second-order wave theory, assuming a smooth transition in the region between the depths at which each theory is applicable. Although these

curves include a second approximation, which was shown by Dore [14] to be erroneous since the outer boundary layer was not accounted for, comparison with experimental results shows the prediction of features not anticipated on the basis of linear theory.

Calculation of the Mass Transport Velocity

Two approaches were used in determining the mass-transport velocity: a Lagrangian method, in which the motion of marker points was followed, and an Eulerian method, in which the mass-transport velocity was calculated from the stream function distribution.

(a) *The Lagrangian Method*

A regular, rectangular array of $m * n$ test points, at n different heights above the surface, is set up at the start of each run. The mass-transport velocity is found from the motion of the points in the velocity field, calculated using the second-order time-stepping procedure described above for the convection of discrete vortices. Over one period T, the points follow an elliptical path, superimposed on which is a steady drift parallel to the surface. The drift $d_{i,j}$ of each point, and hence the mean mass-transport velocity $U_M(y=y_j)$, can be found at each height:

$$U_M(y=y_j)=\frac{1}{m}\sum_{i=1}^{m}\frac{d_{i,j}}{T}. \tag{19}$$

(b) *The Eulerian Method*

For small-amplitude linear waves, Longuet-Higgins [12] obtained the following first approximation to the mass-transport velocity:

$$U_M = U_{M1} + U_{M2} + U_{M3} \tag{20a}$$

$$U_{M1} = \varepsilon^2 \bar{u}_2 \tag{20b}$$

$$U_{M2} = \varepsilon^2 \overline{\int^t u_1\, dt' \frac{\partial u_1}{\partial x}} \tag{20c}$$

$$U_{M3} = \varepsilon^2 \overline{\int^t v_1\, dt' \frac{\partial u_1}{\partial y}} \tag{20d}$$

where the bars denote mean values with respect to time. The velocity vector $\mathbf{u}=(u, v)$ has been expanded in terms of the small parameter ε:

$$\mathbf{u} = \varepsilon \mathbf{u}_1 + \varepsilon \mathbf{u}_2 + \cdots. \tag{21}$$

Terms of higher order than second have been neglected. If the stream function ψ is also expanded in terms of ε, Eqs. (20c) and (20d) can be written

$$U_{M2} = -\varepsilon^2 \overline{\frac{\partial^2 \psi_1}{\partial x \partial y} \int^x \frac{\partial \psi_1}{\partial y} dx'} \tag{22a}$$

$$U_{M3} = \varepsilon^2 \overline{\frac{\partial^2 \psi_1}{\partial y^2} \psi_1}. \tag{22b}$$

When the flow reaches a steady state, Eqs. (22) can be replaced by

$$U_{M2} = \frac{-\varepsilon^2}{c} \overline{\frac{\partial^2 \psi_1}{\partial x \partial y} \int^x \frac{\partial \psi_1}{\partial y} dx'} \tag{23a}$$

$$U_{M3} = \frac{\varepsilon^2}{c} \overline{\frac{\partial^2 \psi_1}{\partial y^2} \psi_1} \tag{23b}$$

where c is the wave speed. The bar now denotes spatial averaging in the x direction at a fixed time. U_{M2} and U_{M3} are obtained by solving Eqs. (23a) and (23b), expressed in finite difference form, on the mesh containing the stream function distribution. Before being applied to Eqs. (23), the stream function at each mesh point is averaged over several time steps. Figure 9 illustrates the process; a second mesh is used, defined within a frame of reference in which the wave is stationary.

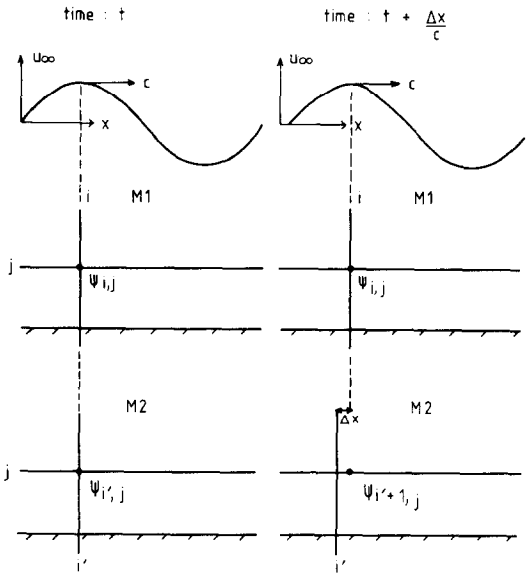

FIG. 9. The phase-averaged stream function ψ_{ij}, at the mesh point (i, j) of mesh M_1, moving in the positive x direction with the wave speed c, obtained by superimposing the vorticity distribution of the stationary mesh M_2 at each of N time steps.

In the present method, errors in the finite difference approximation to third- and fourth-order derivatives of the stream function limited the calculation of mass-transport velocity to second-order terms. No such error, however, was involved in the calculation of $\bar{u}$, the mean Eulerian velocity. $\bar{u}$ can be obtained by summing the circulations Γ_i of all discrete vortices below height y:

$$\bar{u}(y) = -\sum_{y_i < y} \frac{\Gamma_i}{L_x}. \tag{24}$$

An alternative method is that also adopted by Longuet-Higgins; given the stream function distribution ψ, the mean Eulerian velocity can be found directly from the vorticity equation (25), if it is assumed that ψ represents a steady-state solution, so that ψ and ω are periodic.

The vorticity equation in 2-dimensional form is

$$\frac{\partial \omega}{\partial} + (\mathbf{u} \cdot \nabla)\,\omega = \nu \nabla^2 \omega. \tag{25}$$

Taking mean values with respect to time,

$$\overline{[\omega]} + \overline{(\mathbf{u} \cdot \nabla)\,\omega} = \overline{\nu \nabla^2 \omega}. \tag{26}$$

If ω is periodic, the first term in Eq.(26) is zero, and $\bar{\omega}$ is equal to the first derivative of $\bar{u}$ normal to the surface. If ω and u are written in terms of ψ, from Eqs. (26), (3), and (4), $\bar{u}$ is given by

$$\bar{u}(y) = -\frac{L}{\pi \delta^2 c} \int_0^y \overline{\left(\frac{\partial \psi}{\partial y} \cdot \frac{\partial}{\partial x} - \frac{\partial \psi}{\partial x} \cdot \frac{\partial}{\partial y} \right) \nabla^2 \psi}\, dy^3 \tag{27}$$

with boundary conditions

$$\bar{u} = 0 \qquad (y = 0) \tag{28a}$$

$$\frac{d\bar{u}}{dy} \to 0 \qquad (y \to \infty) \tag{28b}$$

$$\frac{d^2 \bar{u}}{dy^2} = 0 \qquad (y = 0). \tag{28c}$$

Equation (27), in finite difference form, is solved numerically on the rectangular mesh containing the time averaged distribution of ψ.

Mass Transport Due to Linear Waves

(a) *Irrotational Flow*

Stokes' irrotational calculation of fluid motion under small amplitude waves in deep water predicts a mass-transport velocity profile given by

$$U_M = \frac{\sigma(a_1 k)^2 \cosh(2ky)}{2k \cosh^2(y_1 k)} \tag{29}$$

where a is the sinusoidal wave amplitude at a height y above the bottom.

In order to compare computed mass-transport velocity with Stokes' theory, the bottom surface was represented by an infinite vortex sheet, a single wavelength section of which was modelled by a row of 80 segments. Eqs. (3) and (4) were solved at each time step on a rectangular mesh consisting of 33×35 square cells. A rec-

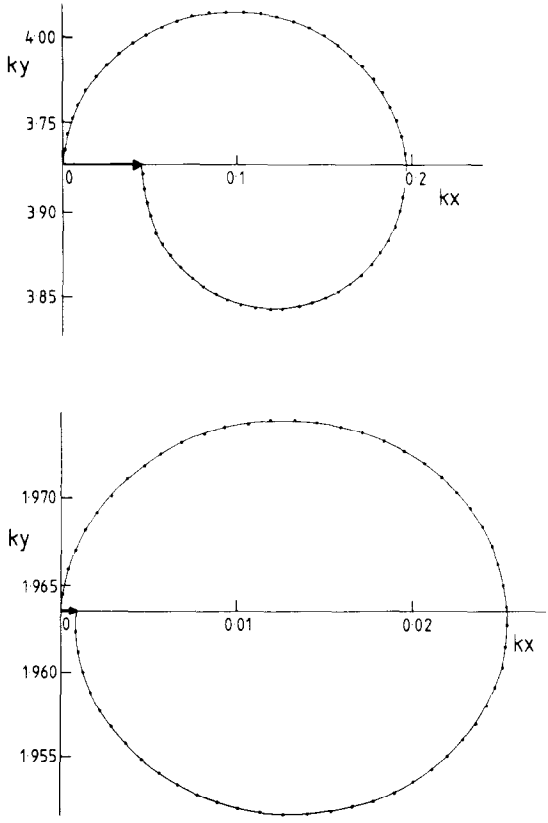

FIG. 10. The paths of two test points, at different heights above the bed, over one cycle of a small amplitude irrotational wave, where $a_1 k = 0.893$, $y_1 k = 5.301$. The arrows show the forward drift of each test point through one cycle.

tangular array of 33×35 test points was used to calculate the mass-transport velocity by the Lagrangian method.

The boundary condition on the stream function gradient, imposed after n time steps at the top of the mesh is given by

$$\left(\frac{\partial u}{\partial y}\right)_{y=y_1} = a_1 \sigma \sin(kx - \sigma n \, \Delta t). \tag{30}$$

The elliptical paths followed by two test points over a single cycle, together with their drift in the positive x direction, are shown in Fig. 10.

Agreement with Stokes theory (Eq. (29)) was found over the range

$$0.6 \lesssim yk \lesssim 3.5$$

$$0.016 \lesssim ak \lesssim 0.134.$$

This is shown in Fig. 11.

The limit of the small amplitude approximation ($ak \ll 1$) is approached at the upper end of this range whereas, at the lower end, the elliptical paths of the test

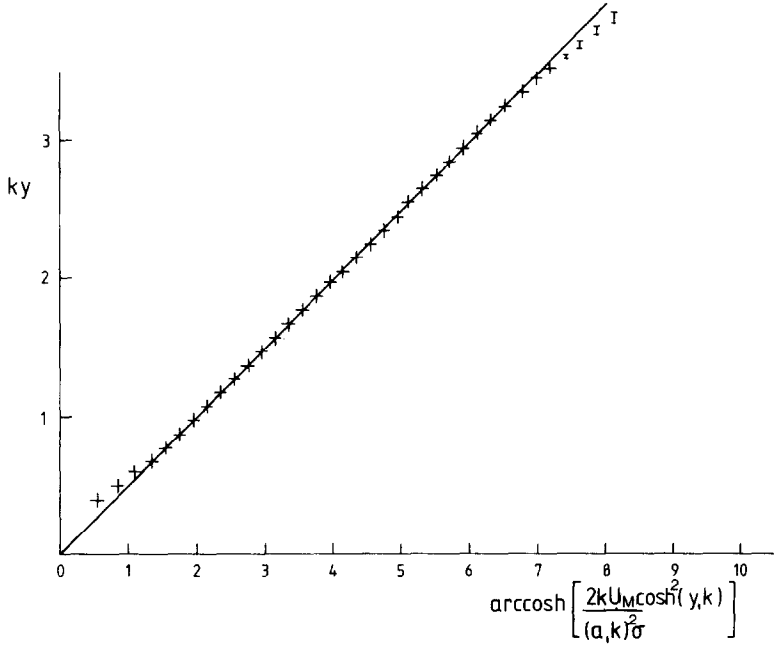

FIG. 11. Variation of arc $\cosh[2kU_M(\cosh^2(y_1k)/(a_1k)^2\sigma]$ with ky for a small-amplitude irrotational wave, where $a_1k = 0.893$, $y_1k = 5.301$. U_M has been calculated from the mean forward drift, at each height, of an array of test points: (—) = linear wave theory; (+) = computational results.

points become small with respect to the cell size and errors in the velocity calculation significantly affect their motion.

(b) *Within the Bottom Boundary Layer*

Comparison was next made with the predictions of Longuet–Higgins [12]; the mass-transport velocity within the bottom boundary layer is given by

$$U_M \frac{k}{\sigma} = \frac{(ak)^2}{4} [5 - 8 \exp(-y/\delta) \cos(y/\delta) + 3 \exp(-2y/\delta)]. \tag{31}$$

The theory assumes first that the boundary layer is sufficiently thin that the wave

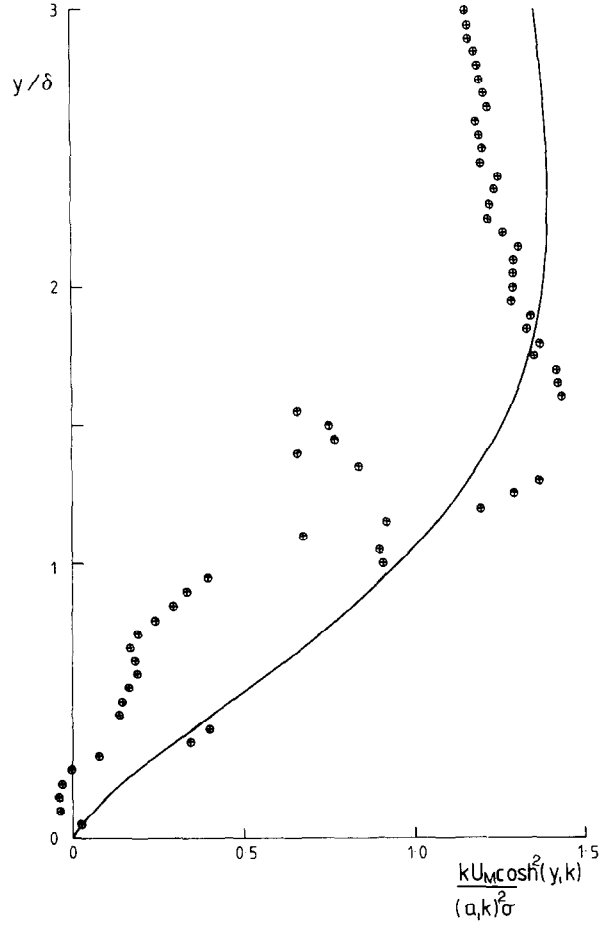

FIG. 12. Variation of $[kU_M \cosh^2(y_1 k)/(a_1 k)^2 \sigma]$ with y/δ for a progressive wave for which $a/L = 0.20$ and $\delta/L = 3.1 \times 10^{-3}$. U_M has been calculated from the average forward drift of an array of test points through the second cycle following the onset of motion: (—) = theory (Longuet-Higgins); (⊕) = computational results.

amplitude, given by irrotational wave theory, does not vary significantly across $\delta(k\delta \ll 1)$, and second that linear wave theory can be applied to the first-order motion of fluid outside the boundary layer ($ak \ll 1$). No restrictions are placed upon the ratio of wave amplitude to boundary-layer thickness.

A mesh was used which expanded exponentially in the y direction. Strong transient effects occur during the first cycle, as the viscous boundary layer becomes established. The mass-transport velocity profile was therefore calculated by following the motion of a regular rectangular array of test points during the second cycle after the onset of the flow. Fig. 12 shows a mass-transport velocity profile calculated

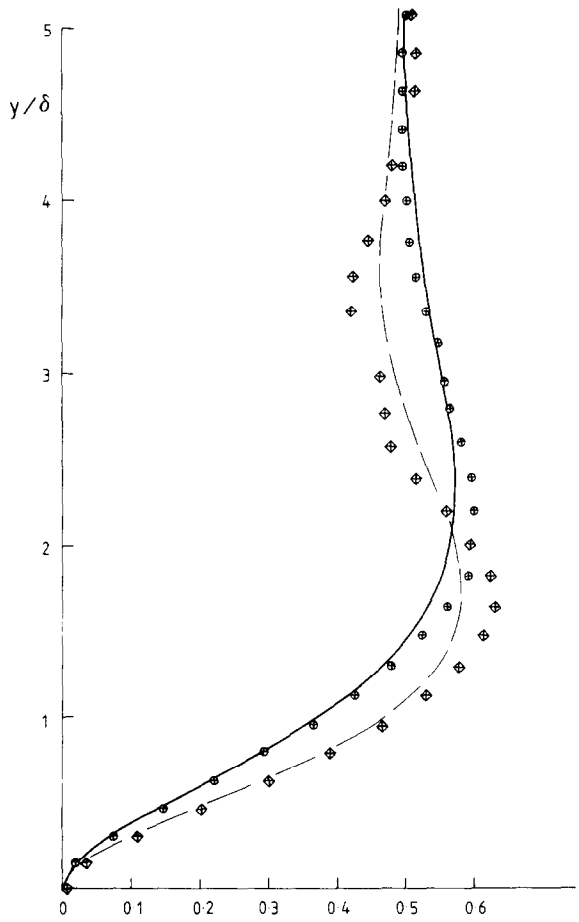

FIG. 13. Variation of $[k/\sigma(a_1k)^2]\ U_{M2}$ and $[k/\sigma(a_1k)^2](U_{M2}+U_{M3})$ with y/δ. The terms U_{M2} and U_{M3} have been calculated from the stream-function distribution, averaged over the second cycle following the onset of motion: $[k/\sigma(a_1k)^2]\ U_{M2}$, (—) = theory (Longuet-Higgins), while (⊕) = computational results; for $[k/\sigma(a_1k)^2](U_{M2}+U_{M3})$, (---) = theory (Longuet-Higgins), while (⊕) = computational results.

in this way. The results contained considerable scatter. Although the mean displacement of the test points in the y direction was zero, individual points were found to drift by amounts of order δ, indicating the presence of transient starting effects.

Equations (20) show that the expression for the mass-transport velocity can be separated into terms U_{M2} and U_{M3} which are functions of the first-order velocity components u and v, and a term U_{M1} which is equivalent to the mean second-order Eulerian velocity in the x direction. Dore [14] showed that the oscillatory boundary layer, inside which the first-order vorticity is confined and determines the profiles of U_{M2} and U_{M3}, is established rapidly after the onset of the flow. An outer boundary layer, which is produced by second-order vorticity diffusing into the flow and thus determines U_{M1}, is established more slowly. Computational profiles of U_{M2} and U_{M3} were evaluated by applying Eqs. (23) to a stream-function distribution, obtained by averaging over the second cycle. A profile is given in Fig. 13 for the case of $a=0$, and comparison made with the theoretical predictions of Longuet-Higgins:

$$U_{M2} = a^2\sigma k[0.5 + 0.5\exp(-2y/\delta) - \exp(-y/\delta)\cos(y/\delta)] \tag{32a}$$

$$U_{M3} = a^2\sigma k[y\exp(-y/\delta)(\sin(y/\delta) + \cos(y/\delta))/2\delta - 0.5\exp(-y/\delta)\sin(y/\delta)]. \tag{32b}$$

In the case of waves with non-zero amplitude, agreement with the predictions of Longuet-Higgins was obtained in the range

$$0 \leqslant ak \lesssim 0.2.$$

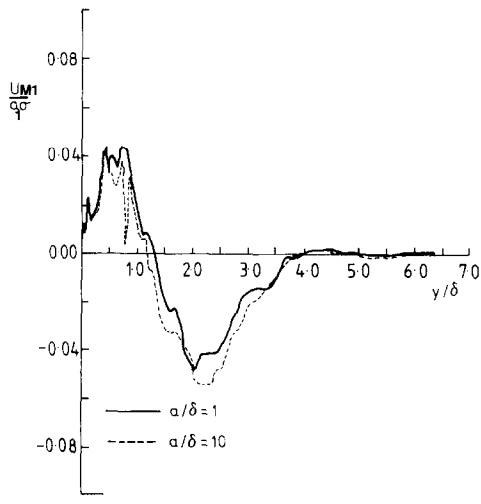

FIG. 14. Profiles of $U_{M1}/a_1\sigma$, for two cycles following the onset of motion, for different values of a/δ.

U_{M1} was calculated at each time step from Eq. (24). Its order of magnitude in the theory of Longuet-Higgins is

$$\frac{U_{M1}}{a\sigma} = O(ak).$$

At small amplitudes, numerical errors are dominant in the computed values of $U_{M1}/a\sigma$. These errors are approximately independent of amplitude, as shown in Fig. 14, and are about 0.05 throughout the first two cycles. These errors become small when

$$ak \gg 0.05.$$

Agreement with the predictions of Longuet-Higgins should therefore be expected in the range

$$0.05 \ll ak \ll 1.$$

Computer runs were performed with values of ak up to 0.5. The results are shown in Fig. 15. The mass-transport velocity profiles approach the theoretical prediction as the outer boundary layer, containing the second-order vorticity, becomes large with respect to δ. The rate of convergence increases with amplitude. At the largest amplitude considered, convergence required approximately 3.5 cycles.

Fig. 16 shows that a closer agreement with theory, as well as a reduction in the required CPU time and memory, can be obtained by solving Eq. (27) using the stream-function distribution, averaged over the second cycle. The influence of starting vortices was reduced by linearly increasing the wave amplitude from zero to its final value through the first quarter cycle of each run. The mass-transport velocity at the top of the boundary layer was found to be slightly dependent upon the value of $(\partial u/\partial y)_{y=y_1}$ used in the application of boundary condition (28b).

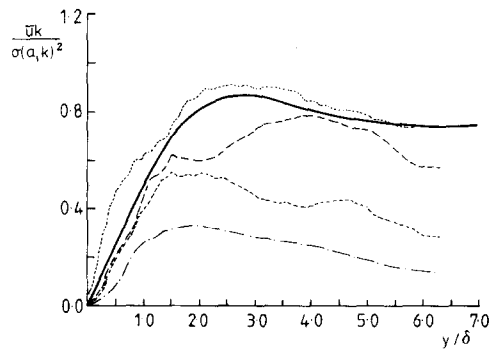

FIG. 15. Profiles of $\bar{u}k/\sigma(a_1k)^2$ taken at intervals throughout the first 3.5 cycles following the onset of motion, where $a/\delta = 250$: (—) = steady-state solution (Longuet-Higgins); (– · – · –) = 1 cycle; (– – –) = 2 cycles; (– – –) = 3 cycles; (· · ·) = 3.5 cycles.

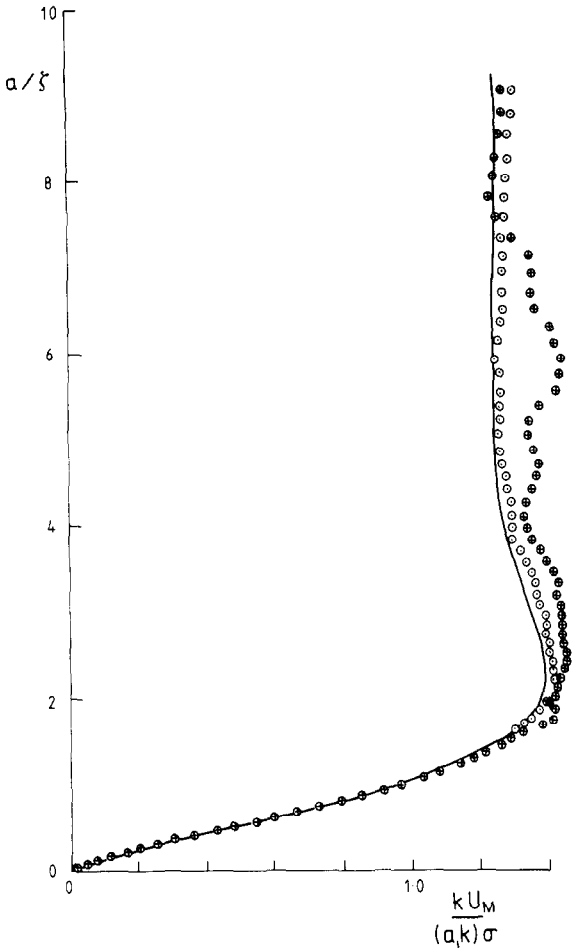

FIG. 16. Profiles of $U_M k/\sigma(a_1 k)^2$. U_M is evaluated from the stream-function distribution, averaged over the second cycle following the onset of motion: (—) = theory (Longuet-Higgins); (⊕) = wave motion started impulsively; (⊙) = wave amplitude increased linearly from zero through the first quarter cycle.

$(\partial u/\partial y)_{y=y_1}$ was taken to be an average value through the upper part of the flow field; the results were influenced by the range of y chosen for this average. In no case, however, did the difference between theory and computational results exceed 4%.

Mass Transport due to Finite Amplitude Waves

The Fourier series/stream-function approach of Rienecker and Fenton [8] can be used to determine the properties of steady irrotational waves of almost arbitrary

height H and period T travelling over a flat bed at any depth d. It is applicable to all waves other than those approaching the solitary wave limit. A program [17] was available which, for given values of H, T, and d, calculates the horizontal velocities at uniformly spaced points lying at a particular height above the bed. These provide the upper boundary condition required to model the viscous diffusion of vorticity from the bed and the subsequent development of a boundary layer. Following Isaacson [16], the mass transport velocity, expressed in the form of the dimensionless group $U_M/((h/d)^2\ (gd)^{1/2})$, is shown in Fig. 17 plotted against $(d/gT^2)^{1/2}$ for different values of H/d. The curves, taken from Isaacson, use cnoidal theory for shallow water and Stokes theory for deep water, with a smooth transition assumed between the two. They are in rough agreement with experiment, which shows considerable scatter, although the deviation from linear theory is clear. Computational values of $U_M/((h/d)^2\ (gd)^{1/2})$ become greater than those in Isaacson's curves as H/d increases, suggesting the importance of modelling finite wave amplitude in shallow water conditions.

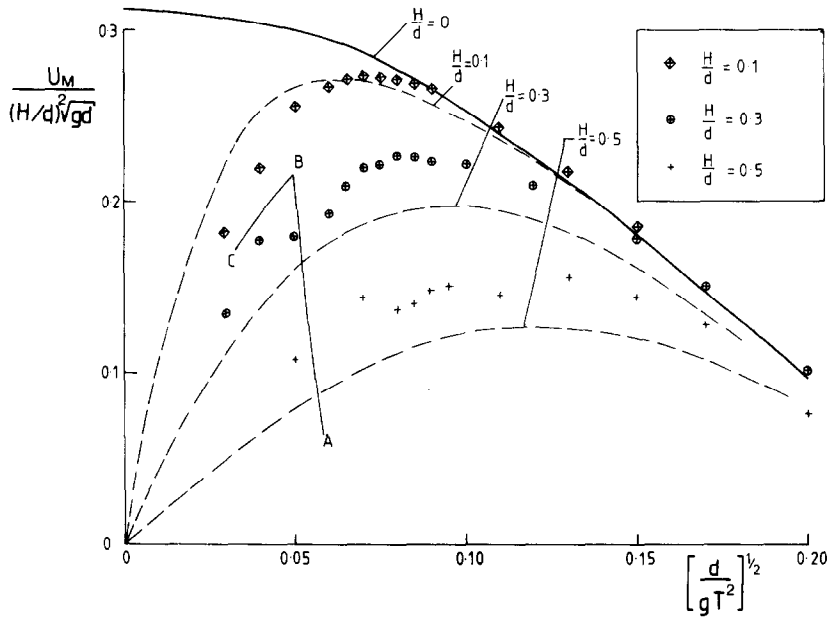

FIG. 17. Comparison of the variation of $U_M/(H/d)^2\sqrt{(gd)}$ with $(d/gT^2)^{1/2}$ as predicted by cnoidal and Stokes' theories (broken lines) with values generated by the vortex model (discrete points). The solid line corresponds to linear wave theory (Longuet-Higgins). The region to the left of line AB, and below BC is that within which $\lambda/d \geqslant 20$ and $H/\lambda \geqslant 0.01$. Under these conditions the waves approach the solitary wave limit and the Rienecker and Fenton method ceases to be applicable.

Small Amplitude Undulations

Fig. 18 shows profiles of U_{M2} and U_{M3} generated by sinusoidal waves over a rippled bed. In a realistic simulation of the sea bed, the wavelength of the ripples 1 would be much smaller than that of the wave L_x. However, since a length L_x of the bed must be discretised into linear segments and the number of segments must be sufficient to define each ripple, the ratio of L_x to 1 was limited to approximately 10. The crest-to-trough distance of the ripples was made equal to δ, so that the flow would remain attached throughout the wave cycle. A range of values of a/δ was investigated. It was found that the limiting values of U_{M2} and U_{M3} were independent of a/δ, although the height above the bed at which these values were approached increased with a/δ.

A profile of U_{M1} could not be obtained from Eq. (27), since the position $y=0$ cannot be defined in the case of a rippled bed. To a second order of approximation, however, U_{M1} is equal to the mean Eulerian velocity, the time development of which is shown in Fig. 19. Although the profile shows considerable irregularity, the results are broadly similar to those shown in Fig. 15 for the case of a plane bed, with the profile tending towards that prediced by Longuet-Higgins for the steady state.

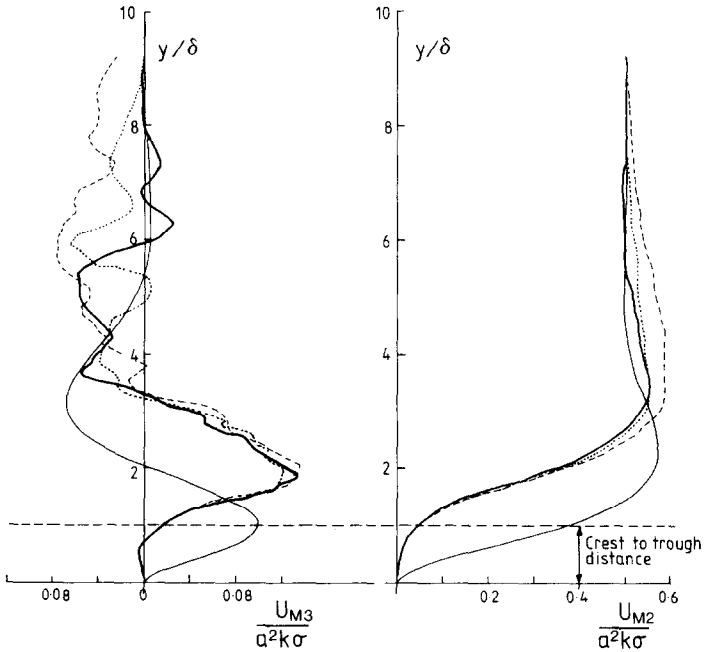

FIG. 18. Profiles of $[U_{M3}/(a^2k\sigma)]$ and $[U_{M2}/(a^2k\sigma)]$ for sinusoidal waves of differing amplitude over a rippled bed: (—) = theory (Longuet-Higgins); (—) = $a/\delta = 1$; (- - -) = $a/\delta = 50$; (– – –) = $a/\delta = 100$.

Sinusoidal Flow over a Rippled Bed

DuToit and Sleath [18] made detailed velocity measurements over smooth rippled beds of fixed form performing sinusoidal oscillations, so that the x coordinate of each position on the bed varies as:

$$X = a \sin(\sigma t) \tag{33}$$

They considered values of a/l ranging from 0.2, giving laminar flow conditions, to 1.2, where the flow was turbulent.

The vortex-in-cell method was used to produce velocity predictions for the case of laminar flow. Following DuToit and Sleath, the bed was set up with a surface profile given by

$$\frac{y}{h} = \frac{\cos(k\xi)}{2} \qquad \frac{x}{h} = \frac{-\sin(k\xi)}{2}.$$

They had shown that this profile is very similar to the mean profile taken by a bed consisting of free grains of sand.

The influence matrix was calculated, as before, for an infinite symmetrical 2-dimensional body, for which the rippled bed formed the upper surface. Suitable numerical parameters for the computations were estimated, for a given set of flow parameters, by varying each one independently until the stream-function distribution at the end of one wave cycle became independent of its value. The set of flow parameters,

$$a/l = 0.2; \qquad \delta/l = 7.96 \times 10^{-3}; \qquad h/l = 0.17,$$

where h is the crest-to-trough distance, required a mesh consisting of 33 elements

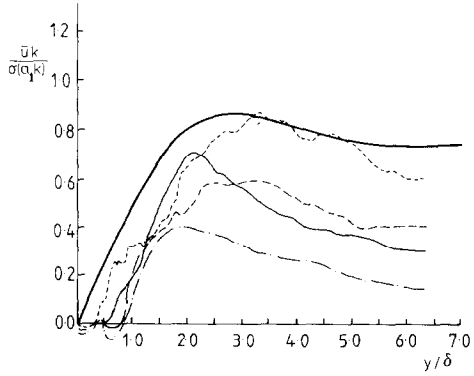

FIG. 19. Profiles of $\bar{u}k/\sigma(a_1 k)^2$ taken at intervals throughout the first 3.5 cycles following the onset of sinusoidal wave motion over a rippled bed, where $a/\delta = 250$; (——) = steady state solution (Longuet-Higgins). (– · – · – · –) = 1 cycle (——) = 2 cycles (– – – –) = 3 cycles (- - - - -) = 3.5 cycles.

(in x) by 65 (in y). Forty discrete vortices were generated per time step, and each wave cycle was subdivided into 56 time steps.

The computations simulated wave motion above a fixed bed. In order to make comparisons with the velocity measurements of DuToit and Sleath, which were made at fixed points above a moving bed, velocities were calculated, using Eqs. (5), at a point moving sinusoidally in the x direction and situated directly above a ripple crest every half wave cycle. The onset-flow velocity was then subtracted from the results.

The calculated velocities were non-periodic. Following the first wave cycle, velocity fluctuations of increasing amplitude occured due to the presence of large eddies, which formed in the lee of each ripple crest and then persisted in the flow near the bed over several cycles. Following Kiya *et al.* [19], a decay law was employed to govern the circulation of each discrete vortex,

$$\frac{\Gamma}{\Gamma_0}(t) = 1 - \exp\left(\frac{-D}{\sigma t}\right), \tag{34}$$

where t is the age of the vortex, Γ_0 is its initial circulation, and D is an empirically determined decay factor. Equation (34) is chosen because it is an exact solution to the Navier–Stokes equations governing the viscous decay of a single vortex. With a

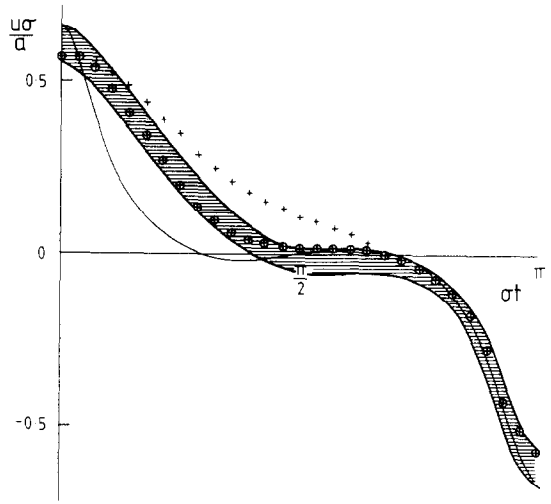

FIG. 20. The velocity cycle at a fixed point above a rippled bed. The bed performs sinusoidal oscillations; the point at which the velocity is calculated lies directly above a ripple crest when $\sigma T = 0$, π,.... Its height y_p above the crest is equal to 3.1δ. Computational results, obtained using different decay factors D, are compared with the experimental results of DuToit and Sleath, and with the potential flow solution, calculated numerically from the velocity potential $\phi = -a\sigma\zeta\cos(\sigma t)$. Experimental results are drawn as a band, corresponding to experimental error: (—) = potential flow; (+) = $D = \pi$; (⊕) = $D = 0.3\pi$.

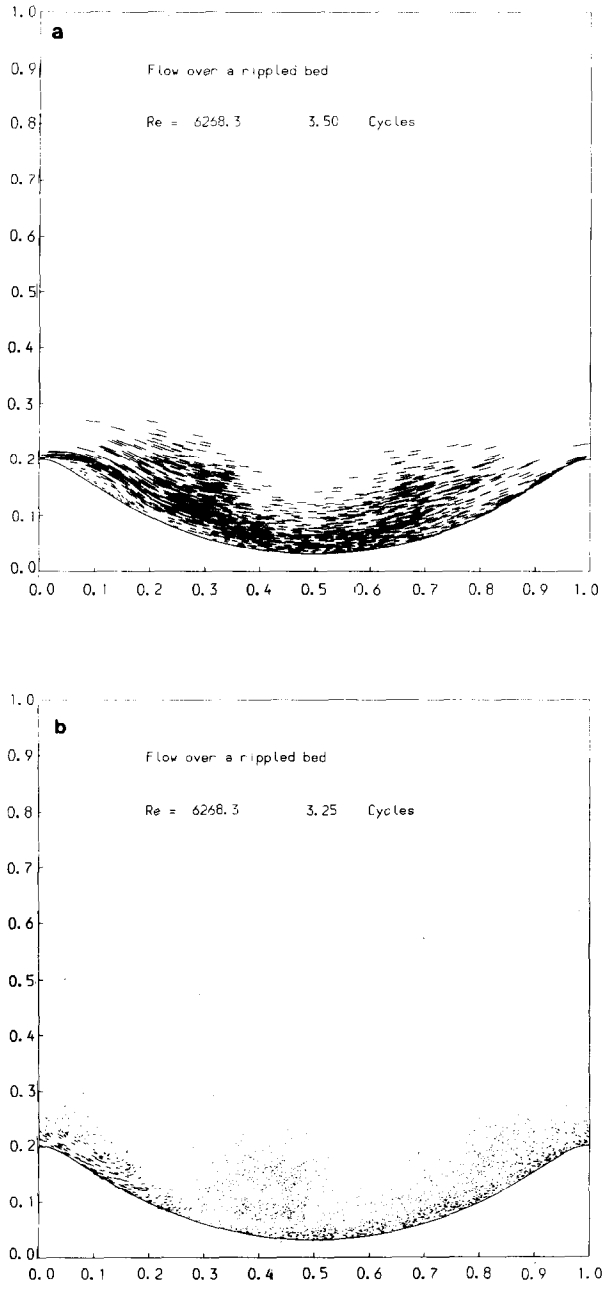

FIG. 21. Sinusoidal flow over a rippled bed at 3.25 and 3.50 cycles following the onset of motion. The Reynolds number Re is defined as $\mathrm{Re} = a\sigma l/\nu$. The diagram shows the paths through which discrete vortices are convected in a single time step. One in four of the total number of vortices is plotted.

suitable decay factor, the influence of the large eddies was diminished, and a periodic flow was obtained after approximately one wave cycle.

Average velocity cycles were calculated; Fig. 20 shows one such cycle at two different values of D. As D is reduced, the potential flow solution is approached. Agreement with experiment, within the limits of experimental error, is obtained at $D = 0.3\pi$, corresponding to a reduction in circulation of 55 % for a vortex in its first quarter cycle. Figure 21 shows the flow patterns obtained at 3.25 and 3.5 cycles following the onset of the flow. These patterns are constructed by drawing the paths through which discrete vortices are convected in a single time step. An eddy in the lee of the ripple crest and separation near the crest can be seen.

Discussion

The representation of the bed by a vortex sheet through a boundary integral

the bed is that it should be periodic. Arbitrary wave motion may be imposed; the only input required is the horizontal velocity distribution at a single level, at a height sufficient for the horizontally varying effects of bed undulations and the boundary layer to be negligible. The number of vortices contained within the flow field increases linearly with time, but the resulting large numbers can be handled efficiently by the use of the vortex-in-cell method, with fast Fourier transforms.

Quantities calculated from the averaged flow field are well predicted (steady-state mass-transport velocity profiles are determined to within 4 %). The phase averaged velocity cycles for separated flows above a rippled bed showed good agreement with experiment, provided a decay factor was incorporated. Instantaneously calculated quantities do, however, show large fluctuations, which is to be expected with the use of random walks. Numerical smoothing of results may be used to better represent physical processes.

In the case of the rippled bed, the use of a regular rectangular mesh means that definition within the boundary layer is poor, with approximately two cells across the boundary layer thickness. Increasing the definition by using a larger mesh did not, however, influence the calculated velocity cycles. This is consistent with results for flows around a cylinder. Attached flows may be simulated without the use of any empirical constant. However, when the flow separates over the rippled bed, a suitably chosen decay factor is required to bring results into agreement with experiment. This is probably required to compensate for large scale 3-dimensional effects which are known to occur for laminar as well as turbulent flows when there is separation. Such a factor was not required for the cylinder flows where the wake quickly convects away from the surface. This does not, however, occur for the rippled bed with zero mean onset flow. The time development of large scale 3-dimensional effects is complex and could depend on a number of external factors, including end conditions. The decay factor is thus simply a tuning device. This dis-

cussion is also pertinent to the modelling of turbulent flows, which are often assumed 2-dimensional and employ empirical turbulence factors. Adjusting factors for turbulence characteristics could in fact be compensating for large-scale 3-dimensional effects in a nominally 2-dimensional situation.

REFERENCES

1. A. J. CHORIN, *J. Fluid Mech.*, **57** (1973), 785.
2. A. J. CHORIN, *J. Comput. Phys.* **27** (1978), 428.
3. D. P. TELIONIS, "Unsteady Viscous Flows," Springer-Verlag, New York, 1981.
4. P. K. STANSBY AND A. G. DIXON, *Appl. Ocean Res.* **5** No. (1983), 167.
5. J. P. CHRISTIENSEN, *J. Comput. Phys.* **13** (1973), 363.
6. G. R. BAKER, *J. Comput. Phys.* **31** (1979), 76.
7. A. G. DIXON AND P. K. STANSBY, "The Cloud-in-Cell Method of Flow Simulation with Surface Vorticity Distributions," Report NW/M/1.3B/1, North West Universities Consortium for Marine Technology, 1983.
8. M. M. RIENECKER AND J. D. FENTON, *J. Fluid Mech.* **104** (1981), 119.
9. H. SCHLICHTING, "Boundary-Layer Theory," 7th Ed., McGraw–Hill, London, 1979.
10. L. M. MILNE-THOMSON, "Theoretical Hydrodynamics," 4th Ed., MacMillan & Co., London, 1962.
11. G. G. STOKES, *Trans. Cambridge Philos. Soc.* **8** (1847), 441.
12. M. S. LONGUET-HIGGINS, *Philos. Trans. R. Soc. London A* **245** (1953), 535.
13. B. D. DORE, *Q. J. Mech. Appl. Math.* **30** (1977), 157.
14. B. D. DORE, *Coastal Eng.* **6** (1982), 93.
15. M. DE ST. Q. ISAACSON, *J. Fluid Mech.* **74** (1976), 401.
16. M. DE ST. Q. ISAACSON, "*ASCE J. Waterw. Port, Coastal Ocean Div.* **104** (1978), 215.
17. G. Y. BUSS AND P. K. STANSBY, "SAWW—A Computer Program to Calculate the Properties of Steady Water Waves," Simon Engineering Labs. Report, University of Manchester, England, 1982.
18. C. G. DUTOIT AND J. F. A. SLEATH, *J. Fluid Mech.* **112** (1981), 71.
19. M. KIYA, K. SASAKI, AND M. ARIE, *J. Fluid Mech.* **120** (1982), 219.